Acoustic response for nonlinear, coupled multiscale model containing subwavelength designed microstructure instabilities

Stephanie G. Konarski, Michael R. Haberman, and Mark F. Hamilton

Phys. Rev. E **101**, 022215 — Published 19 February 2020

DOI: 10.1103/PhysRevE.101.022215

Acoustic response for nonlinear, coupled multiscale model containing subwavelength designed microstructure instabilities

Stephanie G. Konarski*

U.S. Naval Research Laboratory, Code 7165,

Washington, DC 20375

Michael R. Haberman and Mark F. Hamilton

Applied Research Laboratories and Walker Department of Mechanical Engineering,

The University of Texas at Austin,

Austin, Texas 78713

Abstract

Non-periodic arrangements of inclusions with incremental linear negative stiffness embedded within a host material offer the ability to achieve unique and useful material properties on the macroscale. In an effort to study such types of inclusions, the present work develops a time-domain model to capture the nonlinear dynamic response of a heterogeneous medium containing a dilute concentration of subwavelength nonlinear inclusions embedded in a lossy, nearly incompressible medium. Each length scale is modeled via a modified Rayleigh-Plesset equation, which differs from the standard form used in bubble dynamics by accounting for inertial and viscoelastic effects of the oscillating spherical element and includes constitutive equations formulated with incremental deformations. The two length scales are coupled through the constitutive relations and viscoelastic loss for the effective medium, both dependent on the inclusion and matrix properties. The model is then applied to an example nonlinear inclusion with incremental negative linear stiffness stemming from microscale elastic instabilities embedded in a lossy, nearly incompressible host medium. The macroscopic damping performance is shown to be tunable via an externally applied hydrostatic pressure with the example system displaying over two orders of magnitude change in energy dissipation due to changes in pre-strain. The numerical results for radial oscillations versus time, frequency spectra, and energy dissipation obtained from the coupled dynamic model captures the expected response for quasi-static and dynamic regimes for an example buckling inclusion for both constrained and unconstrained negative stiffness inclusions.

* stephanie.konarski@nrl.navy.mil

I. INTRODUCTION

Mechanical metamaterials with designed elastic instabilities have been of increasing interest in recent years. One type of these engineered subwavelength structures achieves the desired negative effective properties through unstable elements, which are described by a fourth-order, non-convex potential energy function [1, 2]. The pioneering work of Lakes and colleagues proved that composite materials with a negative stiffness phase yield extreme material properties that exceed that of its constituents [3–8]. Research on related topics over the last two decades includes analyses on bounds of effective medium moduli and macroscopic stability of materials containing negative stiffness phases [4, 5, 9, 10], ferroelectric materials undergoing a phase transition [6, 7, 11], mass-spring systems [8, 12, 13], and beam structures [14–19].

One application of interest is the ability to efficiently dissipate the mechanical energy of acoustical and vibratory disturbances. The ability to increase damping or provide vibration isolation using nonlinear [20] and quasi-zero stiffness [21] springs has also been long studied, and is often applied to low-frequency vibration isolation systems. More recent efforts include nonlinear energy sinks, where dissipation of vibrations incident on a linear structure is enhanced by transferring the energy to a nonlinear energy sink consisting of a purely cubic nonlinear attachment [22] and further improved with the addition of a negative linear spring component [23]. Increased effective damping has also been demonstrated through buckling elements in single structures [14, 15, 17], periodic lattices [18, 19], layered composites [24, 25], and small-scale inclusions [16, 26–28].

Furthermore, periodic arrangements of mechanical instabilities allow for tunable wave propagation. Geometric and material nonlinearity offer the ability to study small, linear acoustic propagation for large pre-stresses imposed on buckling structures [29–31]. Other metastable systems study the nonlinear propagation of solitary waves [12, 32, 33]. While this offers the ability to create nonreciprocal lattices [31, 34], phononic switches with tunable band gaps [29, 30], and stable propagation through soft lattices [33], these phenomena all currently rely on periodicities of the structure. Of interest in the current work is instead the study of tunable wave phenomena in a heterogeneous medium containing randomly distributed inclusions.

Only a dilute concentration of negative stiffness inclusions may be required to obtain increased damping in a composite material [4, 16]. If the magnitude of the inclusion stiffness is comparable to the surrounding matrix material, the deformation at the inclusion surface is much larger than at the boundary of the composite. The associated high localized strains result in enhanced energy dissipation for a viscoelastic solid [4]. However, previous research on the dynamic behavior of randomly dispersed, negative stiffness inclusions often focus on the quasi-static [4, 16, 17] or low-frequency response [7, 26, 28]. With the advancements in manufacturing methods, the fabrication of complex, small-scale inclusions for acoustic applications [28] is becoming increasingly accessible, which necessitates more advanced, dynamic models that capture the nonlinear, multiscale behavior of these heterogeneous materials.

The present work develops a multiscale material model for a random distribution of negative stiffness inclusions within a matrix material to study the linear and nonlinear dynamics due to an acoustic perturbation. Such dynamic models are not only valuable to predict the macroscopic response, but also for optimization and design purposes to target specific applications. Section II presents the theoretical models used in the present analysis, including the incremental deformation theory and the coupling of an ordinary differential equations utilized at each scale. In Section III, different regimes are explored for an illustrative inclusion design with mechanical instabilities to demonstrate the functionality and validity of the model, including that of an unstable inclusion presented in Section III B and an inclusion constrained within the negative stiffness regime in Section III C.

II. THEORETICAL MODEL

The theoretical model presented in this paper couples concepts of incremental deformation theory [35], multiscale homogenization of a heterogeneous medium containing spherical negative stiffness inclusions [5, 27], and nonlinear dynamics [36, 37] to captures the acoustic response of an effective medium containing a dilute concentration of non-interacting hyperelastic inclusions. The model is applicable to both low and high excitation amplitudes. The macroscale is shown in Fig. 1(a) as an effective medium sphere with radius R_* embedded in a matrix material. The change in radius is determined by the total pressure on the surface of the effective medium sphere P^*_{total}. Within the effective medium is a dilute concentration of non-interacting nonlinear inclusions, as depicted by the single inclusion with radius R_{I} within the matrix in Fig. 1(b). Once again, the change in radius is due to the total pressure

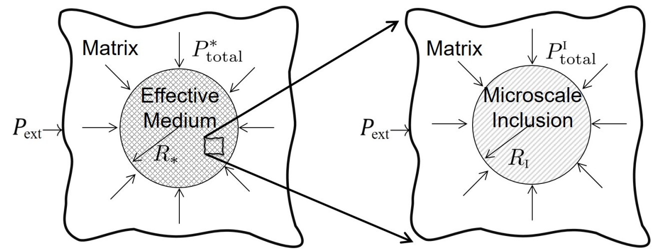

FIG. 1. Schematic for the (a) macroscale showing an effective medium sphere within a matrix being driven by an external pressure P_{ext} and (b) microscale with a single inclusion embedded in a matrix being driven by an external pressure P_{ext}.

on the surface of the inclusion, given by $P^{\text{I}}_{\text{total}}$.

The total pressure on each scale consists of: (*i*) an internal pressure, (*ii*) an effective pressure due to the shear stress of the matrix, and (*iii*) the time harmonic and/or static work done by an external force far away from the surface. For heterogeneous media under isostress conditions, such as suspensions or emulsions, $P^{\text{I}}_{\text{total}} = P^*_{\text{total}}$. The present analysis is currently limited to fluid or fluid-like (nearly incompressible) elastic media for which the isostress assumption is valid. However, for compressible media, the localization of the external forcing pressure on the macroscale to that of the microscale is required.

The dynamic response of a gas bubble in a fluid may be modeled as a forced, nonlinear oscillator through the Rayleigh-Plesset equation. Previous extensions of the Rayleigh-Plesset equation accounted for the effects of a nearly incompressible matrix material [36–38], and the moving mass of an object with non-negligible inertia [39]. The present work further extends the models in Refs [36, 38, 39] to account for the inertial effects and loss mechanism of an oscillating sphere within a matrix through incremental deformation theory. More detail on the modified Rayleigh-Plesset equation utilized here can be found in Ref [27].

In the interest of simplicity, the constitutive relation for the matrix in the present work is equivalent to a linear Kelvin-Voigt material, which in turn is equivalent to the viscoelastic stress tensor developed by Landau and Lifshitz [40]. The corresponding dissipative energy function developed by Landau and Lifshitz [40] may then be incorporated directly in Lagranges equation for a dissipative system. In the case of a nonlinear inclusion embedded in a linear matrix, the result is a Rayleigh-Plesset-type equation for the dynamical response of the inclusion [27, 38].

While the Kelvin-Voigt model of the matrix may not be optimal because it does not account for relaxation, it is a reasonable starting point for investigating the dynamic response of a nonlinear inclusion embedded in a nearly incompressible elastic medium with losses. For example, the Kelvin-Voigt model is used to investigate bubble dynamics in soft tissue, also assumed to be nearly incompressible and lossy [41, 42], and wave propagation through viscoelastic media containing encapsulated, fluid-filled spherical inclusions [43]. Insofar as the focus of the present work is on the nonlinear dynamics of the inclusion, the Kelvin-Voigt model for the surrounding matrix is appealing not only due to its analytical simplicity but also because it reproduces the dissipation term that appears in the much-studied Rayleigh-Plesset equation for bubble dynamics in liquids.

Although the matrix material is simplified in the present work with respect to both the constitutive relationship and loss mechanism, this initial study opens several avenues of future research. For example, future work can explore alternative viscoelastic material models for the matrix based on generalized Kelvin-Voigt, Maxwell, and Zener models [44, 45], or more complex general viscoelastic compressibility to account for viscoelastic loss, and damping due to acoustic radiation loss [46, 47]. Furthermore, the addition of compressibility [37, 48] or use of alternative nonlinear constitutive relationships for the matrix [42] can also be considered. Since the choice of a specific model becomes important for different materials, applications, and regimes of operation, the present work provides an initial basis to pave the way for more complex models in the future.

A. Microscale Dynamics

The form of the Rayleigh-Plesset-type equation solved numerically in the present work for the microscale inclusion is [27]

$$(\rho_{\mathrm{M}} + \rho_{\mathrm{I}}/5)\, R_{\mathrm{I}}\ddot{R}_{\mathrm{I}} + \frac{3}{2}\rho_{\mathrm{M}}\dot{R}_{\mathrm{I}}^2 = P^{\mathrm{I}}_{\mathrm{total}} - (3\zeta_{\mathrm{I}} + 4\eta_{\mathrm{M}})\,\frac{\dot{R}_{\mathrm{I}}}{R_{\mathrm{I}}}, \tag{1}$$

which is a function of the following parameters: the instantaneous density of the inclusion ρ_{I} and the static equilibrium density of the matrix ρ_{M}, which is approximately constant for a nearly incompressible matrix; the instantaneous radius R_{I}, and the first and second time derivatives (denoted with overdots) of the instantaneous radius $\dot{R}_{\mathrm{I}}$ and $\ddot{R}_{\mathrm{I}}$; loss terms related to the imaginary component of the inclusion bulk modulus $\omega\zeta_{\mathrm{I}}$ and matrix shear modulus $\omega\eta_{\mathrm{M}}$; and the total pressure on the surface of the inclusion $P^{\mathrm{I}}_{\mathrm{total}}$. The total pressure is defined by the internal pressure of the inclusion P_{I}, the pressure due to the shear stress of the matrix P_{MI}, and the negative external forcing pressure P_{ext}, such that $P^{\mathrm{I}}_{\mathrm{total}} = P_{\mathrm{I}} + P_{\mathrm{MI}} - P_{\mathrm{ext}}$.

The internal pressure of the inclusion in terms of incremental deformation may be defined using a Taylor series expansion about the pre-strain state (denoted with a subscript 1) [35]:

$$P_{\mathrm{I}} = P_{\mathrm{I1}} - 3K_{\mathrm{I}}\varepsilon_{\mathrm{I}} + \frac{9}{2}K'_{\mathrm{I}}\varepsilon_{\mathrm{I}}^2 - \frac{9}{2}K''_{\mathrm{I}}\varepsilon_{\mathrm{I}}^3. \tag{2}$$

The incremental dimensionless radius $\varepsilon_{\mathrm{I}} = \xi_{\mathrm{I}} - \xi_{\mathrm{I1}}$ is a function of the total and pre-strain dimensionless radii, such that

$$\xi_{\mathrm{I}} = \frac{R_{\mathrm{I}} - R_{\mathrm{I0}}}{R_{\mathrm{I0}}}, \tag{3}$$

$$\xi_{\mathrm{I1}} = \frac{R_{\mathrm{I1}} - R_{\mathrm{I0}}}{R_{\mathrm{I0}}}. \tag{4}$$

Note that ξ_{I} is the small-strain limit of the Green-Lagrange strain tensor necessary to describes finite deformations. The coefficients in the Taylor series are $3K_{\mathrm{I}} = -\,\partial P_{\mathrm{I}}/\partial\xi_{\mathrm{I}}|_{\xi_{\mathrm{I1}}}$, $9K'_{\mathrm{I}} = \partial^2 P_{\mathrm{I}}/\partial\xi_{\mathrm{I}}^2|_{\xi_{\mathrm{I1}}}$, and $27K''_{\mathrm{I}} = -\,\partial^3 P_{\mathrm{I}}/\partial\xi_{\mathrm{I}}^3|_{\xi_{\mathrm{I1}}}$ and represent the local stiffness moduli at the linear, nonlinear quadratic, and nonlinear cubic orders, respectively.

The structurally induced negative stiffness refers to strain states for which $K_{\mathrm{I}} \leq 0$. In addition to the unstable behavior of the inclusion, the dynamics when the inclusion is constrained within the negative stiffness regime is also of interest. Constrained negative stiffness is achievable when the incremental shear modulus of the surrounding elastic matrix material is sufficiently large, i.e. when $K_{\mathrm{I}} + \frac{4}{3}\mu_{\mathrm{M}} \geq 0$ [5, 16]. The present model is limited to either a fluid matrix, or that of a soft viscoelastic solid, for which $\mu_{\mathrm{M}}/K_{\mathrm{M}} \ll 1$. For the case of the solid matrix, an effective pressure characterizes the shear stress on the surface of the inclusion, which may be defined as [27, 36]:

$$P_{\mathrm{MI}} = P_{\mathrm{MI1}} - 4\mu_{\mathrm{MI}}\varepsilon_{\mathrm{I}} + A_{\mathrm{MI}}\varepsilon_{\mathrm{I}}^2 - D_{\mathrm{MI}}\varepsilon_{\mathrm{I}}^3, \tag{5}$$

where μ_{MI} is the local shear modulus and A_{MI} and D_{MI} are the local elastic coefficients at quadratic and cubic order, respectively, for a nearly incompressible medium evaluated at the surface of the inclusion. The local moduli,

$$\mu_{\mathrm{MI}} = \frac{\mu_{\mathrm{M0}}}{1 + \xi_{\mathrm{I1}}}, \tag{6}$$

$$A_{\mathrm{MI}} = \frac{11\mu_{\mathrm{M0}} + A_{\mathrm{M0}}}{(1 + \xi_{\mathrm{I1}})^2}, \tag{7}$$

$$D_{\mathrm{MI}} = \frac{2\,(18\mu_{\mathrm{M0}} + 5A_{\mathrm{M0}} + 8D_{\mathrm{M0}})}{(1 + \xi_{\mathrm{I1}})^3}. \tag{8}$$

are expressed explicitly in terms of the static shear modulus μ_{M0}, and third- and fourth-order elastic constants, A_{M0} and D_{M0}, respectively, of the matrix.

B. Macroscale Dynamics

The ordinary differential equation used to model the macroscale dynamics is of the same form as Eq. (1), where subscripts denoting the inclusion now refer to the effective medium. Several parameters (density, stiffness, and loss) describing the macroscale are obtained via volume-averaging homogenization methods, which inherently couple the two scales by virtue of the functional dependence on the inclusion and matrix properties. The effective density is independent of the dynamics and may be defined from a quasi-static approximation as follows:

$$\rho_* = \phi\rho_{\mathrm{I}} + (1-\phi)\,\rho_{\mathrm{M}}, \tag{9}$$

where $\phi = N(R_{\mathrm{I}}/R_*)^3$ is the instantaneous volume fraction that varies as a function of deformation. The effective medium pressure is assumed to be of the same form as the microscale inclusion,

$$P_* = P_{*1} - 3K_*\varepsilon_* + \frac{9}{2}K_*'\varepsilon_*^2 - \frac{9}{2}K_*''\varepsilon_*^3, \tag{10}$$

where K_*, K_*', and K_*'' are the local linear and nonlinear stiffness moduli and ε_* is the dimensionless change in radius. When a dilute concentration of elastic inclusions, i.e. where the volume fraction $\phi \ll 1$, is embedded in a nearly incompressible matrix with $\mu_{\mathrm{M}} \ll K_{\mathrm{M}}$, it is reasonable to assume that the effective medium is fluid-like and shear effects may be neglected on the macroscale. The homogenization model chosen here is that described in Refs. [27], but others may also be applied as long as they correspond to the same limiting assumptions required for the modified Rayleigh-Plesset type equation. The effective medium sphere is contained within a matrix material of the same constitutive form as Eq. (5)–(8), where the strains correspond to that of the macroscale.

The final source of coupling between scales appears in the macroscopic bulk viscosity ζ_*. It is assumed that ζ_{I} is a constant, but ζ_*, which represents the effective dissipation due to the internal oscillations of the microscale inclusions, is a function of $\dot{R}_*$.

The bulk viscosity of the effective medium may be expressed as

$$\zeta_* = \frac{1}{3}N\left(3\zeta_{\mathrm{I}} + 4\eta_{\mathrm{M}}\right)\frac{R_{\mathrm{I}}\dot{R}_{\mathrm{I}}^2}{R_*\dot{R}_*^2}, \tag{11}$$

which will vary as a function of the deformation through the radial terms of both the inclusion and effective medium.

When accounting for the influence of the inclusion on the effective medium, the ordinary differential equation describing the macroscale is

$$(\rho_{\rm M} + \rho_*/5)\, R_* \ddot{R}_* + \frac{3}{2}\rho_{\rm M} \dot{R}_*^2 = P^*_{\rm total} - 4\eta_{\rm M} \frac{\dot{R}_*}{R_*} - N\left(3\zeta_{\rm I} + 4\eta_{\rm M}\right) \frac{R_{\rm I}\dot{R}_{\rm I}}{R_*^2} \frac{\partial R_{\rm I}}{\partial R_*}, \tag{12}$$

where $P^*_{\rm total} = P_* + P_{{\rm M}*} - P_{\rm ext}$. The derivative of $R_{\rm I}$ with respect to R_* in the final term of Eq. (12) characterizes the influence of the changing radius (or volume) of the inclusion on the radius (or volume) of the effective medium, and is obtained numerically in the present work.

The unknowns obtained by solving the coupled system defined by Eqs. (1) and (12) are the radii on each scale.

The coupled, multiscale model derived in this section is capable of capturing the dynamic behavior of both the micro- and macroscales for propagating acoustic waves. However, the model is also applicable to the case of dynamic loading on the macroscale, which does not necessarily result in a propagating wave. The latter is particularly relevant to vibration isolation and damping applications, which demonstrates the versatility of the present model.

C. Energy Dissipation

It is also of interest to quantify the effective damping of the heterogeneous medium due to the inclusion dynamics. For linear viscoelastic media driven by a time-harmonic forcing function, metrics of damping are clearly defined, such as the phase lag between an applied stress and the associated strain response. However, an analogous definition is not applicable to nonlinear media. Instead, damping is often characterized by energy dissipation, such as specific damping capacity Ψ, because it valid for both linear and nonlinear media and systems[14, 25]. The general definition of damping capacity is energy dissipated over one cycle normalized by stored energy. However, the meaning of stored energy is not as well defined. It has been previously defined as the stored energy in one quarter cycle [14], the maximum stored energy per cycle [49], the work done per cycle [49], and the average stored energy over a cycle [25]. In the present work, the maximum stored energy over one time period is employed. In the limit of linear materials with small damping, the maximum stored energy corresponds to one quarter cycle, but for nonlinear media, the maximum is not necessarily within the first quarter of the time period.

The total energy dissipated at the surface of the effective medium as a function of time is defined as [40]

$$U_{\text{diss}}\left(t\right) = -4\pi\left(3\zeta_{*} + 4\eta_{\text{M}}\right)R_{*}\dot{R}_{*}^{2}. \tag{13}$$

The instantaneous energy stored at time t is defined by [36]

$$U_{\text{str}}\left(t\right) = -4\pi\int_{R_{*}(t)} R_{*}^{2}(P_{*} + P_{\text{M}*})\mathrm{d}R_{*}. \tag{14}$$

The specific damping capacity is then obtained over each period, $T = 1/f_d$,

$$\Psi = \frac{\int_T U_{\text{diss}}\mathrm{d}t}{\int_T U_{\text{str}}\mathrm{d}t} \tag{15}$$

with the dissipated and stored energy obtained from Eqs. (13) and Eq. (14), respectively. Given that the nonlinear inclusions may dissipate or store different amounts of energy per cycle, the specific damping capacity is not necessarily constant as a function of time and will be evaluated over each time period.

III. NUMERICAL SIMULATION OF AN EXAMPLE INCLUSION

To illustrate the capabilities of the coupled multiscale model, the resulting dynamic behavior is explored for one example metamaterial inclusion. A dilute concentration, $\phi_0 = 0.5\%$, of the example inclusions are embedded in a surrounding matrix, of which two example cases are considered. The first is comprised of unstable inclusions within a fluid matrix with $\mu_{\text{M}0} = 0$ Pa, and corresponds to an effective medium with macroscopic instabilities. The second case consists of an inclusion embedded in a lossy, nearly incompressible matrix material with $\mu_{\text{M}0} = 280$ kPa. The shear modulus is large enough to constrain the inclusion within the negative stiffness regime and denotes macroscopic stability for all deformation states in the latter example.

All other properties of the matrix other than the shear modulus remain identical in the two cases, for which the properties are approximately that of water: $\rho_{\text{M}} = 1000$ kg/m^3 and $K_{\text{M}} = 2.2$ GPa, which are commonly chosen values approximately equal to those of water [43, 50]. Additionally, in both cases the bulk viscosity of the inclusion is zero, such that $\zeta_{\text{I}} = 0$, but the shear viscosity of the matrix is non-zero, at $\eta_{\text{M}} = 5$ Pa·s, which is in

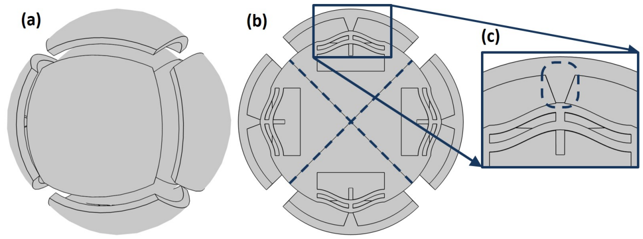

FIG. 2. Example of an unstable metamaterial inclusion design with beam elements as (a) full sphere, (b) cut of full sphere to reveal internal features, and (c) zoomed in of the double beam elements with the pressure transformer denoted with a dashed box.

the vicinity of the values discussed in the literature for nearly incompressible viscoelastic media [43, 50].

Each multiscale system is subjected to a sinusoidal forcing pressure, $p = p_a \sin(f_d \tau / f_0)$, where p_a is the amplitude of the acoustic pressure wave, f_d is the drive frequency in Hz, f_0 is the undamped natural frequency at the global equilibrium position in Hz, and $\tau = 2\pi f_0 t$ is dimensionless time. The value of f_d/f_0 is chosen to be 0.1 in all cases to ensure that resulting behavior is subresonant at each pre-strain to ensure the macroscale approximation is valid. The driving pressure amplitude p_a will vary in each case.

The constitutive response of both the example inclusion and the effective medium in the low-frequency limit for both matrix materials are explored in Section III A. The subresonant response is obtained for unstable inclusions in Section III B and for the inclusions exhibiting constrained negative stiffness in Section III C. In each case, three pre-strains are discussed to exhibit the changing behavior as a function of inclusion deformation and illustrate the tunable nature of the example metamaterials. These pre-strains are introduced in Section III A.

A. Snapping acoustic metamaterial inclusion

A three-dimensional schematic of the inclusion of interest appears in Fig. 2(a), where a cut of the sphere is shown in (b) to reveal the internal features. The inclusion is symmetric about the cut plane, as well as the dashed lines shown in Fig. 2(b). The symmetry lines partition the inclusion into four quadrants in-plane. Within each quadrant there is a double beam element, a pressure transformer, and a curved outer surface that interfaces with the matrix. The zoomed in figure of Fig. 2(c) more clearly shows the double beam elements, where the pressure transformed is highlighted in the dashed box. An external force incident on the inclusion-matrix interfaces is concentrated at the pressure transformer to deform the center of the double beam elements. The desired response is obtained due to the double beam elements, which are introduced instead of single beam elements to ensure the second buckling mode of the clamped-clamped beam is constrained [51].

The example inclusion utilized in the present work has initial radius of $R_{\mathrm{I}0} = 29.5$ mm and is constructed out of nylon. A finite element method (FEM) model for the element shown in Fig. 2 is developed using Comsol Multiphysics. In the model, the displacement is imposed on the pressure transformers to compress the beam elements. Then, the strain energy density of the entire element resulting from that deformation is calculated in Comsol. The results of that model represent a displacement-controlled loading where the resulting strain energy density exhibits two inflections points that induce the desired mechanical instabilities.

From the strain energy density versus displacement FEM results, the pressure P_{I} and strain E_{I} is obtained, as shown in Fig. 3(a). There exist strain states for which the pressure-strain curve has a negative slope, corresponding to positive linear stiffness, strain states where there is a positive slope representing negative linear stiffness, and strain states with zero slope with zero linear stiffness. The vertical dashed lines denote the states of zero linear stiffness, where the negative stiffness regime falls between the two lines. Dashed lines corresponding to the same strain states also appear in the deformation-dependent linear stiffness K_{I} shown in Fig. 3(b). Several pre-strain states are denoted in Fig. 3(a) and (b). Pre-strain A (solid circle) represents the global equilibrium configuration for which there is no deformation. Pre-strain B (solid triangle) is approximately at the first pressure extremum in Fig. 3(a), which corresponds to $K_{\mathrm{I}} \approx 0$ in Fig. 3(b). Pre-strain C (solid square) represents a point within the negative stiffness regime.

In displacement-controlled loading, the deformation moves through all strain states, including those within the negative stiffness regime. However, for pressure-controlled loading, when the inclusion reaches state B, the inclusion undergoes a large deformation due to a small change in pressure, commonly referred to as snap-through behavior. After the snap-through, the inclusion is now constrained to state E (open triangle), which represents the same internal pressure, but a different strain value. The same behavior is observed upon unloading the system. State D (open square) represents the same pressure as state C, but

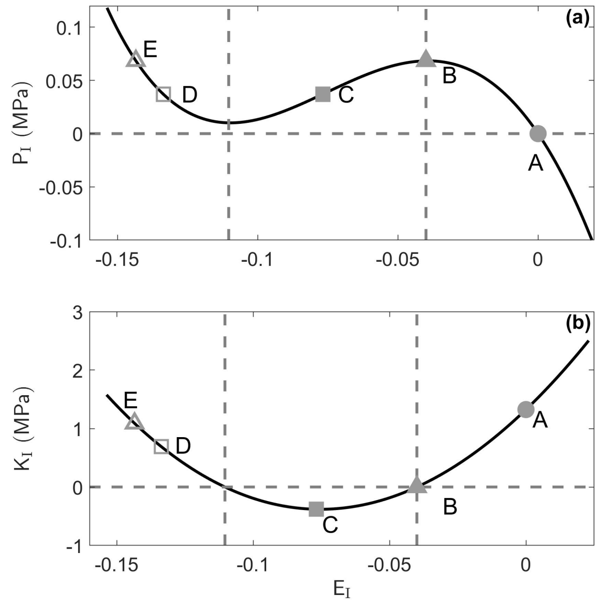

FIG. 3. (a) Inclusion pressure P_{I} in MPa versus strain E_{I} and (b) local linear stiffness K_{I} in MPa versus strain E_{I}. The three initial pre-strains of interest are denoted by A (solid circle), B (solid triangle), and C (solid square). Pre-strain state D (open square) represents the same pressure but at different strain value as state C, and state E (open triangle) represents the same pressure but different strain as state E. The linear negative stiffness region of the inclusion is delineated by the gray dashed lines.

with a different strain value. Although the pressure amplitudes are the same for states B and E, and states C and D, respectively, in Fig. 3(a), the stiffnesses in (b) differ. For state B, $K_{\mathrm{I}} \approx 0$, and for state C, $K_{\mathrm{I}} < 0$. However, states D and E represent local linear stiffnesses values that are distinctly positive and greater than zero.

It is of interest to explore the dynamics of two different effective media, one with a fluid matrix and one with a viscoelastic matrix. The effective medium pressure P_* versus strain E_* is shown in Fig. 4(a) for $\mu_{\mathrm{M0}} = 0$ Pa (solid) and $\mu_{\mathrm{M0}} = 280$ kPa (dotted). The corresponding local linear stiffness K_* as a function of strain E_* is shown in Fig. 4(b). The effective medium pressure versus strain response for $\mu_{\mathrm{M0}} = 0$ Pa in Fig. 4(a) is non-monotonic and the pressure amplitude resembles that of the inclusion shown in Fig. 3(a). The similarity is expected because a fluid matrix offers no shear resistance to the macroscopic deformation. Therefore, there exists a local regime of negative stiffness on the macroscale, as illustrated

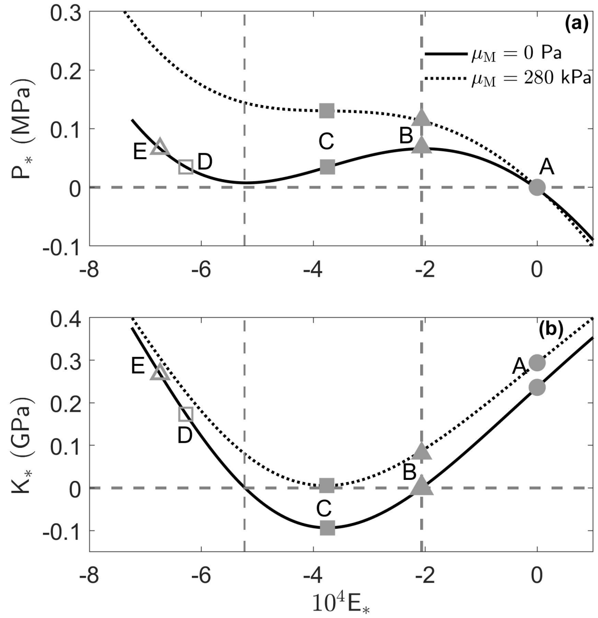

FIG. 4. (a) Effective medium pressure P_* in MPa versus strain E_* and (b) local linear stiffness K_* in GPa versus strain E_* for two different shear moduli, $\mu_{\rm M0} = 0$ Pa (solid line) and $\mu_{\rm M0} = 280$ kPa (dotted line). The three initial pre-strains of interest are denoted bu A (solid circle), B (solid triangle), and C (solid square). Pre-strain state D (open square) represents the same pressure but at different strain value as state C, and state E (open triangle) represents the same pressure but different strain as state E. The linear negative stiffness region of the inclusion is delineated by the gray dashed lines.

by the solid line in Fig. 4(b). The region between the vertical dashed corresponds to the microscale negative stiffness regime, which is identical to the strain states for macroscopic negative stiffness. When the shear modulus is increased to $\mu_{\rm M0} = 280$ kPa, the corresponding pressure curve in Fig. 4(a) becomes monotonic and has shifted up in magnitude relative to $\mu_{\rm M0} = 0$ Pa. This implies that the macroscale is stable for all strain states and characterizes an effective medium with constrained negative stiffness on the microscale. The local linear stiffness K_* has shifted upward for $\mu_{\rm M0} = 280$ kPa relative to at $\mu_{\rm M0} = 0$ Pa and is now purely positive.

The same strain states A-E from Fig. 3 are again highlighted in Fig. 4(a) and (b). States A (solid circle), B (solid square), and C (solid triangle) are indicated for both shear moduli, and represent the three initial pre-strain states for which the dynamics are considered. Although the pressures are the same at the global equilibrium given by state A, the local stiffness on the macroscale differ for the two cases considered due to the differences in slope in the pressure-strain curve. For the effective medium where $\mu_{\mathrm{M0}} = 0$ Pa, pre-strain B represents the local pressure extremum, where $K_* \approx 0$ and pre-strain C corresponds to a state within the macroscopic negative stiffness regime. As with the inclusion, states D (open square) and E (open triangle) represent the same pressure but different strain values as pre-strains C and B, respectively, for an effective medium with $\mu_{\mathrm{M0}} = 0$ Pa.

For the case with $\mu_{\mathrm{M0}} = 280$ kPa, pre-strains B and C represent points of microscale zero linear stiffness and negative stiffness, respectively. However, the macroscale is fully constrained, so $K_* > 0$ always. Instead, pre-strain B represents a segment of the pressure-strain curve with a decreased local linear stiffness relative to pre-strain A, and pre-strain C possesses a decreased local linear stiffness relative to pre-strain B, but are both still positive. States D and E are not relevant when considering the behavior for an inclusion constrained in a matrix with $\mu_{\mathrm{M0}} = 280$ kPa. The dynamic response is now considered for the fluid matrix in Section III B for initial pre-strains A, B, and C, where states D and E become important, and for a viscoelastic matrix inducing constrained negative stiffness in Section III C for initial pre-strains A, B, and C, where states D and E are relevant to resulting behavior.

B. Unstable Inclusion

The first case considered is that of an unstable inclusion embedded in a fluid matrix material for the three pre-strains A, B, and C denoted in Figs. 3 and 4. Although the inclusion cannot be constrained in the negative stiffness regime, pre-strain C is still considered to explore how the coupled model behaves for instances where macroscopic instabilities are present. In this example, it is assumed that an external mechanism constrains the inclusion within the negative stiffness regime for all time $\tau < 0$, but is removed at $\tau = 0$. The driving pressure amplitude is $p_0 = 500$ Pa.

First consider the normalized radius $R_{\mathrm{I}}/R_{\mathrm{I}}^{\mathrm{int}}$ as a function of dimensionless time τ shown in Fig. 5(a), (b), and (c) for pre-strain A, B, and C, respectively. The radius $R_{\mathrm{I}}^{\mathrm{int}}$ represents the initial radius to which the inclusion is constrained to by external pressure P_0. In Fig. 5(a), the inclusion oscillates with a small amplitude about the imposed pre-strain radius. During

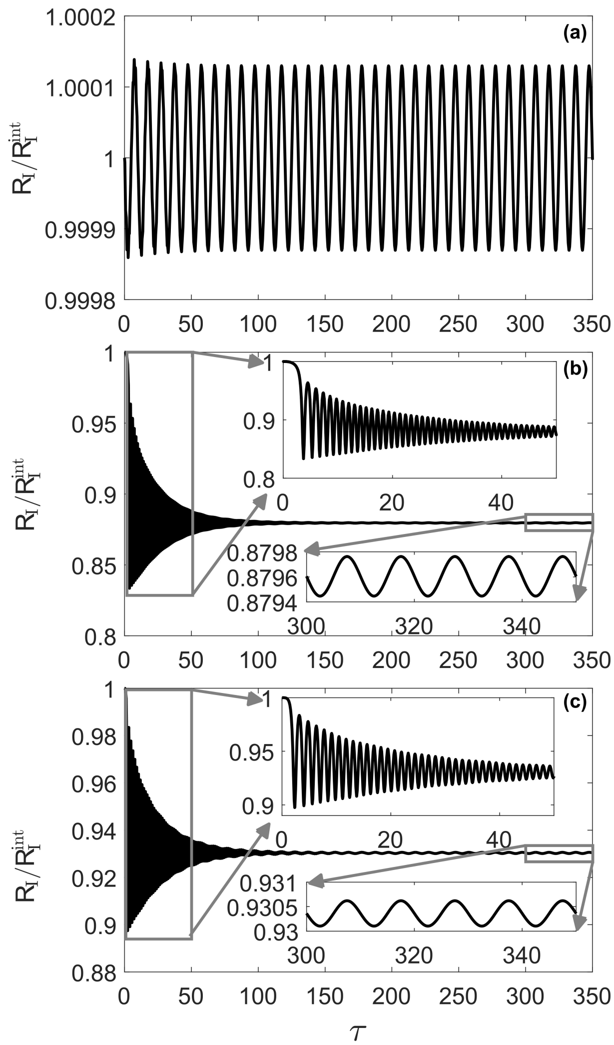

FIG. 5. Normalized radius $R_{\mathrm{I}}/R_{\mathrm{I}}^{\mathrm{int}}$ versus dimensionless time τ for an unstable inclusion in a fluid matrix with properties approximately those of water for (a) pre-strain A, (b) pre-strain B, and (c) pre-strain C. Inserts in (b) and (c) show both the transient and steady-state regimes.

the first few cycles, transient effects are observed, but a steady-state response resembling that of a linear, sinusoidal oscillator is soon reached. Therefore, at this drive amplitude and pre-strain, the inclusion oscillations are small and appear linear.

The behavior at pre-strain B, shown in Fig. 5(b), is much different than for pre-strain A. Two inserts more clearly present the transient behavior, given roughly by $\tau < 300$, and the steady-state behavior, for approximately $\tau > 300$. Initially, the inclusion is constrained to $R_{\mathrm{I}}/R_{\mathrm{I}}^{\mathrm{int}} = 1$ and oscillates a few times about the initial condition before snapping through to a state given by $R_{\mathrm{I}}/R_{\mathrm{I}}^{\mathrm{int}} \approx 0.8796$, which corresponds to state E in Figs. 3 and 4. The initially large oscillations decay with each cycle until a steady-state response is reached. The steady-state response, which also resembles the behavior of a linear, sinusoidal oscillator, is about pre-strain state E.

Inclusions constrained to pre-strain C are also perturbed from the initial condition and the oscillations are about a state other than $R_\mathrm{I}/R_\mathrm{I}^\mathrm{int} = 1$ as shown in Fig. 5(c). When starting in the negative stiffness regime, the inclusion immediately snaps from the initial condition $R_\mathrm{I}/R_\mathrm{I}^\mathrm{int} = 1$ to a smaller radius $R_\mathrm{I}/R_\mathrm{I}^\mathrm{int} = 0.9303$. The new pre-strain is defined by state D in Figs. 3 and 4. The large amplitude oscillations then decay to sinusoidal behavior in steady state, where the oscillations are now about the stable pre-strain D.

Despite the large radial oscillations on the microscale, there is little deformation on the macroscale. The maximum change in radius for pre-strain A is $7.5 \times 10^{-5}\%$. Although the snap-through deformation induces large changes in the microscale radii for pre-strains B and C, the maximum change in radius for the macroscale is within 0.063% and 0.038%, respectively. Therefore, the coupled dynamic model captures that the localized strain on the surface of the inclusion is much larger than the boundary of the effective medium even for large microscale deformations.

To further understand the resulting nonlinearity, the frequency content of the radial oscillations is considered at each pre-strain. However, in the case of the snapping behavior for pre-strains B and C, the spectral behavior is more clearly visualized with a spectrogram obtained via a short-time Fourier transform. The power spectrum amplitude in dB is shown as a function of dimensionless time τ and normalized frequency f/f_d in Fig. 6(a), (b), and (c) for pre-strains A, B, and C, respectively. The amplitude is normalized by the mean magnitude at $f/f_d = 1$. For all cases there is a significant amount of power at zero frequency.

The spectrogram for pre-strain A in Fig. 6(a) indicates most of the power is concentrated near $f/f_d = 1$, confirming the dynamics correspond to a predominately a linear system. The transient response, i.e. for $\tau > 150$, indicates some power at the local undamped natural frequency $f/f_d \approx 10$ is attenuated before reaching a steady-state response. When steady-state is reached, the amplitude is significantly smaller at all frequencies other than at the fundamental drive frequency of $f/f_d = 1$, indicating that the overall system response is predominantly linear.

The spectrogram for pre-strain B, shown in Fig. 6(b), demonstrates a more prominent transient response. The power is mainly concentrated at $f/f_d \approx 10$, which corresponds to

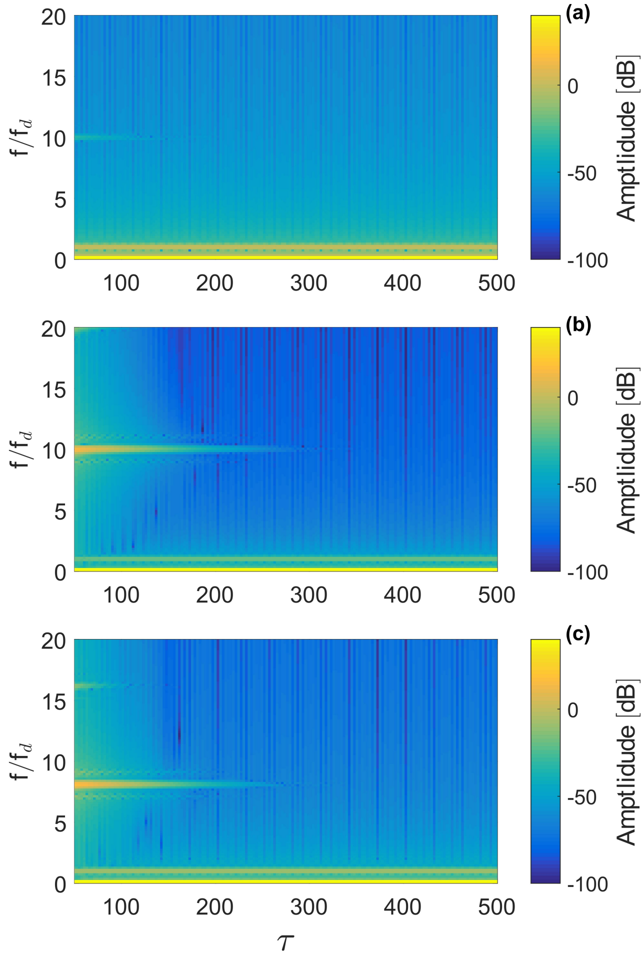

FIG. 6. Spectrogram amplitude in dB as a function of normalized frequency f/f_d and dimensionless time τ for an unstable inclusion in a fluid matrix with properties approximately those of water for (a) pre-strain A, (b) pre-strain B, and (c) pre-strain C.

the local undamped natural frequency at pre-strain E, rather than at pre-strain B. However, energy at the fundamental drive frequency f/f_d is still evident. Additionally, for $\tau < 150$, the spectrum is more broadband and the power is dispersed over the frequency band shown. As the transient behavior decays towards a steady-state solution, the power near $f/f_d = 10$ decreases, but remains relatively constant at f/f_d. The radial oscillations due to snap-through deformation are so large that steady-state is not reached until $\tau > 300$, which then corresponds to a linear sinusoidal response.

A similar trend is observed for pre-strain C, shown in Fig. 6(c). The local undamped natural frequency is that of the new constrained state after snap-through, pre-strain D, for

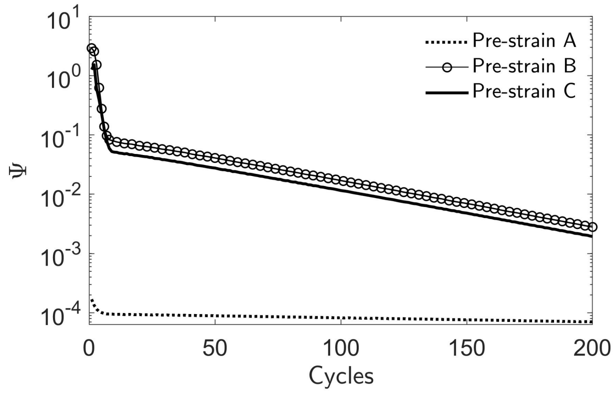

FIG. 7. Damping capacity per cycle for an unstable inclusion in a fluid matrix with properties approximately those of water for pre-strain A (dotted line), pre-strain B (connected open circles) and pre-strain C (solid line).

which $f/f_d \approx 8$. There is a significant amount of power concentrated at the undamped natural frequency, with a small amount also visible at the second harmonic, $f/f_d \approx 16$. The fundamental drive frequency $f/f_d = 1$ is clearly excited in the transient regime, but the power is dispersed across the range of frequencies shown. As time increases, the amplitudes are attenuated except at the drive frequency, indicating a linear, steady-state response.

Since large radial oscillations were obtained when the inclusion snaps from an initial state to a new constrained state, it is also anticipated that a large amount of energy is dissipated relative to the energy stored. The damping capacity per cycle obtained from Eqs. (13)–(15), shown in Fig. 7, exhibits this trend, where the snap-through deformation for pre-strain B (connected open circles) and pre-strain C (solid line) results in an initially large damping capacity greater than 1. After several cycles, the damping capacities of pre-strains B and C approach a much smaller value that continually decreases as the radial oscillations on the macroscale reach steady state. Slightly more energy is dissipated at pre-strain B than C because the snap-through deformation induces a larger change in strain when deforming from pre-strain B to E than when deforming from pre-strain C to D. In both cases, the large displacements due to snap-through will induce a favorable damping capacity relative to pre-strains that are constrained to one stable state.

The high damping observed in this case is a transient phenomenon. As the oscillations of the inclusion reach steady state, the damping capacity will further decrease until it is similar in magnitude to that of Pre-strain A. For this case, the inclusion would need to be continuously reset to an unstable or nearly unstable state to exploit the snap-through deformations for efficient energy dissipation. It may be difficult to reset the structures by passively varying the external pressure, but may be feasible using active components in the inclusions. For example, one can envision a scenario where an externally imposed voltage is used to control the pre-strain of the inclusion that contains electro-mechanically coupled material domains. The inclusion could then be controlled to repeatedly return to the quasi-zero linear stiffness configuration after activation by an external disturbance, such as an acoustic wave that induces snap-through deformation at the microscale. Alternatively, one can also envision control on different time scales using a phase transformation induced via thermo-mechanical loading, as with shape-memory polymers or alloys, and small-scale inclusions could be designed that reset to a desired configuration via an external temperature. The present model is still relevant when studying similar inclusions that utilize other activation methods, and extensions to capture this should be explored in future work.

C. Constrained Negative Stiffness

The case of snapping inclusions constrained within the negative stiffness regime by a nearly incompressible viscoelastic matrix with a sufficiently large shear modulus allows the study of small (and large) perturbations about some constrained reference state for all strains. The three pre-strains are again denoted by A, B, and C in Figs. 3 and 4. In the example presented for a constrained inclusion, the shear modulus is $\mu_{\mathrm{M0}} = 280$ kPa and the driving pressure amplitude is $p_0 = 6$ kPa. All other parameters are identical to the fluid matrix case.

Shown in Fig. 8 is the normalized radius $R_{\mathrm{I}}/R_{\mathrm{I}}^{\mathrm{int}}$ as a function of dimensionless time τ. The normalization allows the induced perturbations to oscillate about $R_{\mathrm{I}}/R_{\mathrm{I}}^{\mathrm{int}} = 1$ such that the steady-state dynamics of all three pre-strains can be conveniently compared. In Fig. 8(a), the steady-state dynamics for pre-strain A resembles a linear sine wave. For pre-strain B in Fig. 8(b), some distortion exists in the sinusoidal shape. The dynamic behavior is not symmetric about the initial radius and instead undergoes more compression than expansion over each cycle of the drive period. Additionally, the peaks and troughs are no longer perfectly rounded. The nonlinearity is most perceptible for the negative stiffness regime, as shown for pre-strain C in Fig. 8(c). The sinusoidal forcing function induces peaks

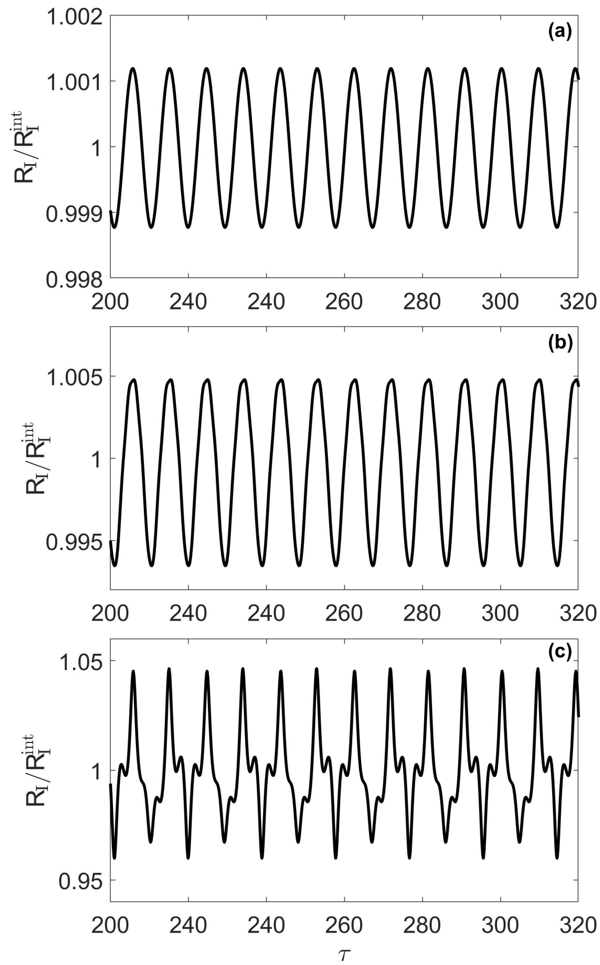

FIG. 8. Normalized radius $R_{\mathrm{I}}/R_{\mathrm{I}}^{\mathrm{int}}$ versus dimensionless time τ in steady state for a constrained inclusion in a viscoelastic matrix with $\mu_{\mathrm{M0}} = 280$ kPa and remaining properties approximately those of water for (a) pre-strain A, (b) pre-strain B, and (c) pre-strain C.

and troughs at the same values of τ as for the pre-strains A and B, but there now exist additional, smaller fluctuations within each period. Closer examination reveals that the nonlinear response repeats over a time scale of two periods of the drive frequency. Lastly, the amplitude for pre-strain B is marginally larger than for pre-strain A, but the maximum amplitude obtained for pre-strain C is an order of magnitude larger than at the other two pre-strains. This implies that the decreased stiffness at pre-strain C, relative to A and B, significantly increases the nonlinearity and maximum perturbation from the constrained reference state for the same source function.

For the constrained negative stiffness case, the dynamic response is dominated by the

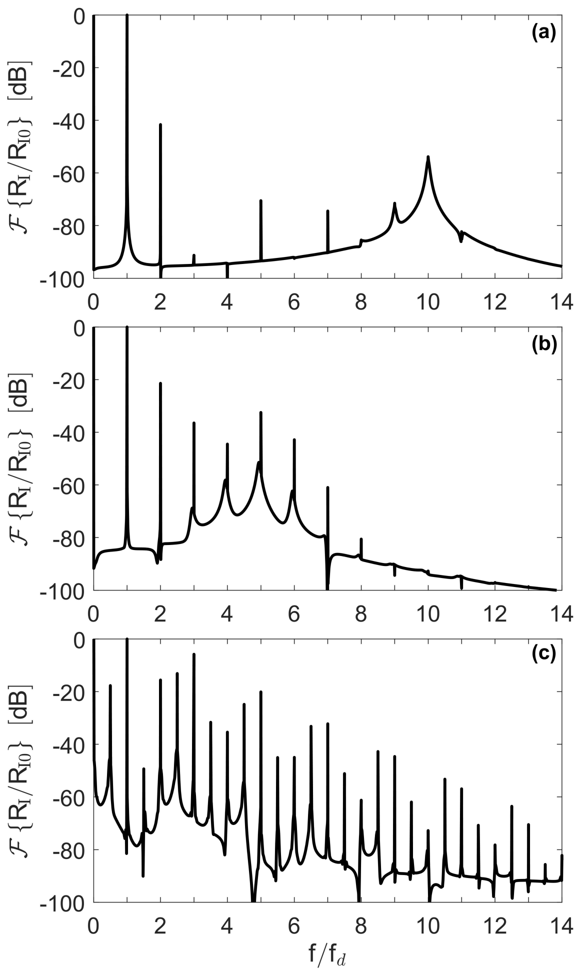

FIG. 9. Normalized spectrum in dB as a function of normalized frequency f/f_d and dimensionless time τ for a constrained inclusion in a viscoelastic matrix with $\mu_{\text{M0}} = 280$ kPa and remaining properties approximately those of water for (a) pre-strain A, (b) pre-strain B, and (c) pre-strain C.

steady-state behavior, and the spectral content is easily understood from the Fourier transform, as shown in Fig. 9. The spectrum $\mathcal{F}\{R_{\text{I}}/R_{\text{I0}}\}$ is normalized such that the amplitude is 0 dB at $f/f_d = 1$. For pre-strain A, the spectral content shown in Fig. 9(a) should resemble that of a linear system due to the sinusoidal oscillations in Fig. 8(a), where the amplitude is concentrated at the fundamental drive frequency. In addition to the narrowband peak at $f/f_d = 1$, a weak second harmonic exists that is approximately 40 dB down from the fundamental, and higher-order harmonics appear that are more than 70 dB down. There also exists a resonance at the local undamped natural frequency ($f/f_d \approx 10$), which is more than 50 dB down, which once again represents a transient effect as is evident from Fig. 6(a). The magnitudes of the harmonics relative to the fundamental reveal that nonlinearity is present in the system when the inclusion is constrained to pre-strain A, but it is barely observable even at a drive amplitude of $p_0 = 6$ kPa. Further increase in the source amplitude would induce nonlinearity even at this pre-strain and cause the generated harmonics to become meaningful contributions to the overall behavior.

The spectral content of pre-strains B and C indicates varying levels of nonlinearity. At pre-strain B, shown in Fig. 9(b), the amplitude of the second harmonic is about 20 dB down from the fundamental, while the third and fifth harmonics, which are approximately 30 dB down from the fundamental, are weaker contributions to the overall response. The relative influence of each harmonic in Fig. 9(b) is consistent with the behavior in Fig. 8(b), which reveals that distortion exists in the sinusoidal response of the radius versus time, but the overall trend resembles that of a linear oscillator.

The case corresponding to the example negative stiffness state in Fig. 9(c) reveals the most nonlinearity. Distinct spectral peaks are observed in $\mathcal{F}\{R_{\mathrm{I}}/R_{\mathrm{I0}}\}$ in addition to the fundamental drive frequency. A strong third harmonic of the drive frequency exists, which is within 6 dB of the fundamental. Other harmonics of the drive frequency also appear at varying amplitudes, but they are all more than 15 dB below the fundamental. Peaks also manifest at non-integer multiples of f_d. Subharmonics occur at frequencies less than the driving frequency and are defined by $f/f_d = 1/(n+1)$ for $n = 1, 2, 3, \ldots$ [52]. Only the first subharmonic, $f/f_d = 1/2$, is present in Fig. 9(c), which is almost 20 dB below the fundamental. Additionally, there are integer half-multiples that occur at frequencies greater than the driving frequency and are defined as $f/f_d = (2n+1)/2$ for $n = 1, 2, 3, \ldots$. Within the field of bubble dynamics, these frequencies are sometimes referred to as a ultraharmonics [52]. In Fig. 9(c), ultraharmonics occur at several frequencies (e.g. $f/f_2 = 3/2, 5/2, 7/2\ldots$) with varying amplitudes. For example, at $f/f_d = 5/2$, the amplitude is approximately 15 dB below the fundamental, but the ultraharmonics at higher frequencies are more than 20 dB down.

Generation of subharmonics and ultraharmonics stems from sufficiently large magnitudes of the driving pressure incident upon a system with strong nonlinearity. At $p_0 = 6$ kPa, it is possible to induce oscillations at frequencies other than integer multiples of the driving frequency. However, this behavior is only observed for inclusions constrained in the negative stiffness regime. The threshold pressure to induce subharmonic or ultraharmonic generation

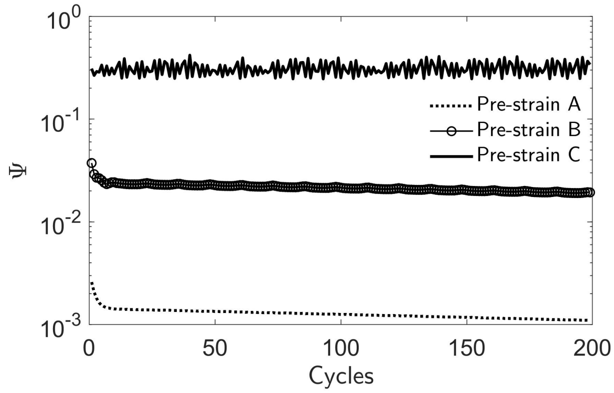

FIG. 10. Damping capacity per cycle for a constrained inclusion in a viscoelastic matrix with $\mu_{\mathrm{M0}} = 280$ kPa and remaining properties approximately those of water for pre-strain A (dotted line), pre-strain B (connected open circles) and pre-strain C (solid line).

is therefore characterized by the amount of nonlinearity present at each pre-strain. For pre-strain C, the threshold is the smallest, and would be larger for pre-strain B, and larger still for pre-strain A. Thus, there is an inverse relationship between the minimum external forcing pressure and maximum macroscopic stiffness necessary to observe subharmonic and ultraharmonic generation. The ability to generate subharmonic and ultraharmonics only at pre-strain C further signifies that a strongly nonlinear response is obtained for an inclusion constrained within the negative stiffness regime relative to the other cases.

Larger radial oscillations are obtained when constrained to the negative stiffness regime relative to other pre-strains, which can be exploited for specific applications such as a energy dissipation. The damping capacity per cycle is shown in Fig. 10. Pre-strain A (dotted line) represents the smallest damping capacity as expected due to the smallest amplitude radial oscillations. The steady-state damping capacity for pre-strain B (open circles) is increased by over an order of magnitude relative to pre-strain A. However, the damping capacity for pre-strain B is more than an order of magnitude smaller than for pre-strain C (solid line). The increased nonlinearity present at Pre-strain C also results in more fluctuation in the damping capacity per cycle than at Pre-strains A and B. Unlike for the unconstrained inclusion, the increase in damping capacity due to microscale instabilities for the constrained inclusion is a steady-state phenomena. The magnitude of the damping capacity for all three cases shown in Fig. 10 therefore changes minimally with the number of cycles.

IV. CONCLUSION

The present work develops a coupled multiscale model to capture the dynamics of nonlinear inclusions embedded in a nearly incompressible matrix material. Each scale is modeled using a modified Rayleigh-Plesset equation, where the scales are coupled through the stiffness, density, and loss of the effective medium. As the local material properties vary on the microscale due to an external forcing pressure, the corresponding effective properties describing the macroscale will also change.

The dynamic model properly captures the snap-through deformation, for which a small pressure perturbation induces a large change in strain. This occurs in the presence of macroscopic instabilities, which are induced when the static shear modulus of the matrix cannot constrain the inclusion, as occurs with a fluid. As the inclusion undergoes large snap-through deformation, a significant amount of energy is dissipated due to the large transient radial oscillations relative to the small, steady-state oscillations about a constrained state. Therefore, this behavior is of interest in applications where energy dissipation is important, such as impact and shock absorption [18].

When the macroscale is stable, a larger time-harmonic pressure amplitude is required to induce nonlinearity than for a matrix with zero shear modulus. A more strongly nonlinear response is achieved in the negative stiffness regime, which results in a larger damping capacity, whereas the nearly linear response occurring for zero pre-strain yields the smallest damping capacity. These results for constrained and unconstrained negative stiffness agree with those reported in the literature for ordered periodic media with metamaterial unit cells [19, 23] or single structures [14, 17], but were instead obtained here via a coupled, multiscale time-domain model for randomly distributed, subwavelength inclusions. In verifying the expected response through this initial study, additional frequency-domain effects and their utility to acoustical applications can be explored in future work, such as harmonic generation, parametric amplification, and phase conjugation.

It is also worth emphasizing that the theoretical model presented here is not specific to the chosen inclusion design or metamaterials in general. While the current model utilized a nearly incompressible viscoelastic medium with a Kelvin-Voigt model, it is possible to also include compressibility of the matrix, as well as other viscoelastic constitutive relationships, which is recommended for future research. The present numerical model is also valuable for design purposes, where the geometric features of the inclusion may be varied to obtain an optimal macroscale response, and to study the effects of pre-stress on similar inclusions that utilize other activation methods such as piezoelectric or thermo-mechanical loading.

ACKNOWLEDGMENTS

This work was supported by the Office of Naval Research. Additional support for the lead author also came from the Chester M. McKinney Graduate Fellowship in Acoustics at the Applied Research Laboratories at The University of Texas at Austin.

---

[1] C. S. Wojnar and D. M. Kochmann, "A negative-stiffness phase in elastic composites can produce stable extreme effective dynamics but not static stiffness," Philos. Mag. **94**, 532–555 (2013).

[2] D. M. Kochmann and K. Bertoldi, "Exploiting microstructural instabilities in solids and structures: From metamaterials to structural transitions," Appl. Mech. Rev. **69**, 050801 (2017).

[3] Y. C. Wang and R. S. Lakes, "Extreme thermal expansion, piezoelectricity, and other coupled field properties in composites with a negative stiffness phase," J. Appl. Phys **90**, 6458–6465 (2001).

[4] R. S. Lakes, "Extreme damping in composite materials with a negative stiffness phase," Phys. Rev. Lett. **86**, 2897–2900 (2001).

[5] R. S. Lakes and W. J. Drugan, "Dramatically stiffer elastic composite material due to a negative stiffness phase?" J. Mech. Phys. Solids **50**, 979–1009 (2002).

[6] R. S. Lakes, T. Lee, A. Bersie, and Y. C. Wang, "Extreme damping in composite materials with negative-stiffness inclusions," Nature **410**, 565–567 (2001).

[7] Y. C. Wang, M. Ludwigson, and R. S. Lakes, "Deformation of extreme viscoelastic metals and composites," Mat. Sci. Eng. A-Struct. **370**, 41–49 (2004).

[8] Y. C. Wang and R. S. Lakes, "Extreme stiffness systems due to negative stiffness elements," Am. J. Phys. **72**, 40–50 (2004).

[9] W. J. Drugan, "Elastic composite materials having a negative stiffness phase can be stable," Phys. Rev. Lett. **98**, 055502 (2007).

[10] D. M. Kochmann and W. J. Drugan, "Analytical stability conditions for elastic composite materials with a non-positive-definite phase," Proc. R. Sco. A **465**, 2230–2254 (2012).

[11] T. Jaglinski, D. Kochmann, D. Stone, and R. S. Lakes, "Composite materials with viscoelastic stiffness greater than diamond," Science **315**, 620–622 (2007).

[12] N. Nadkarni, C. Daraio, and D. M. Kochmann, "Dynamics of periodic mechanical structures containing bistable elastic elements: From elastic to solitary wave propagation," Phys. Rev. E **90**, 023204 (2014).

[13] Z. Wu, R. L. Harne, and K. W. Wang, "Exploring a modular adaptive metastructure concept inspired by muscle's cross-bridge," J. Intell. Mater. Syst. Struct. (2015).

[14] L. Dong and R. Lakes, "Advanced damper with high stiffness and high hysteresis damping based on negative strucutral stiffness," Int. J. Solids Struc. **50**, 2416–2423 (2013).

[15] H. Kalathur and R. S. Lakes, "Column dampers iwth negative stiffness: high damping at small amplitudes," Smart Mater. Struc. **22**, 084013 (2013).

[16] T. Klatt and M. R. Haberman, "A nonlinear negative stiffness metamaterial unit cell and small-on-large multiscale material model," J. Appl. Phys. **114**, 033503 (2013).

[17] S. Cortes, J. Allison, C. Morris, M. R. Haberman, C. Seepersad, and D. Kovar, "Design, manufacture, and quasi-static testing of metallic negative stiffness structures within a polymer matrix," Exp. Mech. **57**, 1183–1191 (2017).

[18] D. M. Correa, T. Klatt, S. Cortes, M. Haberman, D. Kovar, and C. Seepersad, "Negative stiffness honeycombs for recoverable shock isolation," Rapid Prototyping J. **21**, 193–200 (2015).

[19] D. Chronopoulos, I. Antoniadis, and T. Ampazidis, "Enhanced acoustic insulation properties of composite metamaterials having embedded negative stiffness inclusion," Extreme Mech. Lett. **12**, 48–54 (2017).

[20] P. Alabuzhev, A. Gritchin, L. Kim, G. Migirenko, V. Chon, and P. Stephanov, "Vibration protecting and measuring systems with quasi-zero stiffness," (CRC Press, 1989) pp. 7–29.

[21] D. L. Platus, "Negative-stiffness-mechanism vibration isolation system," Vib. Control Microelectron. Opt. Metrol. **1619**, 44–54 (1991).

[22] D. D. Quinn, S. Hubbard, N. Wierschem, M. A. Al-shudeifat, R. J. Ott, J. Luo, B. F. Spencer Jr., D. M. McFarland, A. F. Vakakis, and L. A. Bergman, "Equivalent modal damping, stiffening and energy exchanges in multi-degree-of-freedom systems with strongly nonlinear

attachments," J. Multi-body Dynamics **226**, 122–146 (2012).

[23] M. A. Al-Shudeifat, "Highly efficient nonlinear energy sink," Nonlinear Dyn. **76**, 1905–1920 (2014).

[24] K. Alur and J. Meaud, "Nonlinear mechanics of non-dilute viscoelastic layered composites," Int. J. Solids and Struct. **72**, 130–143 (2015).

[25] T. Sain, J. Meaud, G. Hulburt, E. M. Arruda, and A. M. Waas, "Simultaneously high stiffness and damping in a class of wavy layered composites," Adv. Mater. **27**, 4296–4301 (2013).

[26] J. Bishop and R. L. Harne, "Leveraging the arrangement of multiple, critically constrained inclusions in resonant metamaterials for control of broadband vibroacoustic energy," Appl. Acoust. **130**, 222–229 (2018).

[27] S. G. Konarski, M. R. Haberman, and M. F. Hamilton, "Frequency-dependent behavior of media containing pre-strained nonlinear inclusions: Application to nonlinear acoustic metamaterials," J. Acoust. Soc. Am. **144**, 3022–3035 (2018).

[28] C. Morris, L. Bekker, C. Spadaccini, M. Haberman, and C. Seepersad, "Tunable mechanical metamaterial with constrained negative stiffness for improved quasi-static and dynamic energy dissipation," Adv. Eng. Mater. **21**, 1900163 (2019).

[29] K. Bertoldi and M. C. Boyce, "Wave propagation and instabilities in monolithic and periodically structured elastomeric materials undergoing large deformations," Phys. Rev. B **78**, 184107 (2008).

[30] P. Wang, F. Casadei, S. Shan, J. C. Weaver, and K. Bertoldi, "Harnessing buckling to design tunable locally resonant acoustic metamaterials," Phys. Rev. Lett. **113**, 014301 (2014).

[31] B. M. Goldsberry, S. P. Wallen, and M. R. Haberman, "Non-reciprocal wave propagation in mechanically-modulated continuous elastic metamaterials," J. Acoust. Soc. Am. **146**, 782–788 (2019).

[32] B. Deng, J.R. Raney, V. Tournat, and K. Bertoldi, "Elastic vector solitons in soft architected materials," Phys. Rev. Lett. **118**, 204102 (2017).

[33] J. R. Raney, N. Nadkarni, C. Daraio, D. M. Kochmann, J. A. Lewis, and K. Bertoldi, "Stable propagation of mechanical signal in soft media using stored elastic energy," P. Sci. Acad. Sci. USA **113**, 9722–9727 (2016).

[34] Z. Wu, Y. Zheng, and K. W. Wang, "Metastable modular metastructure for on-demand reconfiguration of band structures and nonreciprocal wave propagation," Phys. Rev. E **97**,

022209 (2018).

[35] R. W. Ogden, “Non-linear elastic deformations,” (Dover Publications, Inc., 1984) pp. 328–336.

[36] S. Y. Emelianov, M. F. Hamilton, Yu A. Ilinskii, and E. A. Zabolotskaya, “Nonlinear dynamics of a gas bubble in an incompressible elastic medium,” J. Acoust. Soc. Am. **115**, 581–588 (2004).

[37] L. A. Ostrovskii, “Nonlinear acoustics of slightly compressible porous media,” Sov. Phys Acoust. **34**, 523–526 (1988).

[38] E. A. Zabolotskaya, Yu A. Ilinskii, G. D. Meegan, and M. F. Hamilton, “Modification of the equation for gas bubble dynamics in a soft elastic medium,” J. Acoust. Soc. Am. **118**, 2173–2181 (2005).

[39] E. A. Zabolotskaya, Yu A. Ilinskii, and M. F. Hamilton, “Weakly nonlinear oscillations of a compliant object buried in soil,” J. Acoust. Soc. Am. **125**, 2035–2040 (2008).

[40] L. D. Landau and E. M. Lifshitz, “Theory of elasticity,” (Pergamon, 1986) pp. 135–140, 3rd ed.

[41] Z. Yang and C. C. Church, “A model for the dynamics of gas bubbles in soft tissues,” J. Acoust. Soc. Am. **118**, 3595–3606 (2005).

[42] R. Gaudron, M. T. Warnez, and E. Johnsen, “Bubble dynamics in a viscoelastic medium with nonlinear elasticity,” J. Fluid Mech. **766**, 54–75 (2015).

[43] A. M. Baird, F. H. Kerr, and D. J. Townend, “Wave propagtion in a viscoelastic medium containing fluid-filled microspheres,” J. Acoust. Soc. Am. **105**, 1527–1538 (1999).

[44] M. T. Warnez and E. Johnsen, “Numerical modeling of bubble dynamics in viscoelastic media with relaxation,” Phys. Fluids **27**, 063103 (2015).

[45] B. Yin, X. Hu, and K. Song, “Evaluation of classic and fractional models as constitutive relations for carbon blackfilled rubber,” J. Elastom. Plast. **50**, 463–477 (1956).

[46] A. Prosperetti and A. Lezzi, “Bubble dynamics in a compressible liquid. part 1. first-order theory,” J. Fluid. Mech. **168**, 457–478 (1986).

[47] Yu. A. Ilinskii and E. A. Zabolotskaya, “Cooperative radiation and scattering of acoustics waves by gas bubbles in liquids,” J. Acoust. Soc. Am. **92**, 2837–2841 (1992).

[48] J. B. Keller and M. Miksis, “Bubble oscillations of large amplitudes,” J. Acoust. Soc. Am. **68**, 628–633 (1980).

[49] G. F. Lee and B. Hartman, “Specific damping capacity for arbitrary loss angle,” J. Sound Vib. **211**, 265–272 (1998).

[50] C. C. Church, "The effects of an elastic solid surface layer on the radial pulsations of gas bubbles," J. Acoust. Soc. Am **97**, 1510–1521 (1994).

[51] J. Qiu, J. H. Lang, and A. H. Slocum, "A curved-beam bistable mechanism," J. Microelectromech. S. **13**, 137–146 (2004).

[52] T. G. Leighton, "The acoustic bubble," (Academic Press Ltd., 1994) pp. 413–424.